Materials and Design 193 (2020) 108807

Contents lists available at ScienceDirect

Materials and Design

journal homepage: www.elsevier.com/locate/matdes

Hollow-structured NiCoP nanorods as high-performance electrodes for asymmetric supercapacitors

Zining Wang [a], Hui Wang [a], Shan Ji [b,*], Xuyun Wang [a], Pengxin Zhou [c], Shuhui Huo [c], Vladimir Linkov [d], Rongfang Wang [a,*]

[a] State Key Laboratory Base for Eco-Chemical Engineering, College of Chemical Engineering, Qingdao University of Science and Technology, Qingdao 266042, China
[b] College of Biological, Chemical Science and Chemical Engineering, Jiaxing University, Jiaxing 314001, China
[c] College of Chemistry and Chemical Engineering, Northwest Normal University, Lanzhou 730070, China
[d] South African Institute for Advanced Materials Chemistry, University of the Western Cape, Cape Town 7535, South Africa

HIGHLIGHTS

- 1D hollow-structured NiCoP nanorods were synthesized via phosphorization.
- Formation of void space in NiCoP nanorods results from Kirkendall effect.
- NiCoP supercapacitor cathode showed an energy density of 68 Wh kg^{-1} at 9594 W kg^{-1}.

GRAPHICAL ABSTRACT

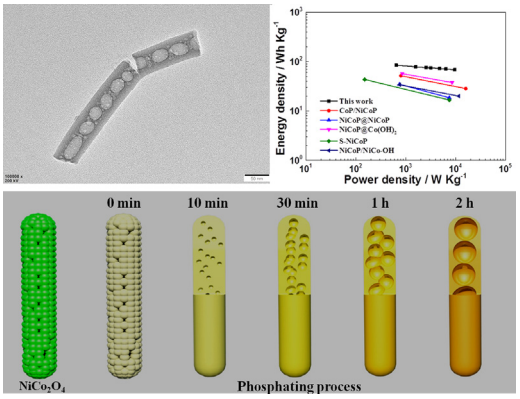

ARTICLE INFO

Article history:
Received 26 March 2020
Received in revised form 9 May 2020
Accepted 11 May 2020
Available online 15 May 2020

Keywords:
NiCoP
One-dimensional
Hollow structure
Kirkendall effect
Energy storage

ABSTRACT

One-dimensional hollow-structured NiCoP nanorods are synthesized via Kirkendall effect resulting from different diffusion rates of Ni and Co ions at 350 °C, using NaH_2PO_2 as a phosphorization agent. Various techniques were used to study the formation mechanism of hollow NiCoP nanorods which structure and crystallinity could be effectively tuned by adjusting phosphorization time. Capacitance of NiCoP reaches 273.4 μAh cm^{-2} at a current density of 30 mA cm^{-2} with a rate retention of 85.6%. Specific capacitance of an asymmetric supercapacitor cell (ASC) where NiCoP sample was used together with activated carbon reached 264.6 μAh cm^{-2} at 2 mA cm^{-2} and decreased to 213.2 μAh cm^{-2} with current density rising to 30 mA cm^{-2}. The ASC possesses quite high energy- and power densities, compared to previously reported results, which demonstrates applicability of hollow NiCoP nanorods for electrochemical energy storage.

* Corresponding authors.
E-mail addresses: jishan@zjxu.edu.cn (S. Ji), rfwang@qust.edu.cn (R. Wang).

https://doi.org/10.1016/j.matdes.2020.108807

1. Introduction

In an ongoing endeavor to alleviate serious environmental problems and global warming caused by fossil fuels, immense research and development efforts have been made worldwide towards integration of energy storage systems with renewable and clean energy sources, such as solar panels and wind turbines [1–3]. However, power output of these renewable energy sources is unpredictable, thus reliable and low-cost energy storage devices are critical for their effective utilization [4,5]. Pseudocapacitors, also called supercapacitors, are emerging as promising devices for renewable systems due to their relatively low cost, high power density and long cycling life [6–8]. The performance of supercapacitors depends on electrochemical efficiency of three kinds of electrodes, such as carbon-based materials, transition metal compounds and conductive polymers [9,10]. Among these, transition metal oxides and hydroxides exhibit specific capacitances at least one order of magnitude higher than those of carbon materials [11,12]. On the other hand, low electrical conductivity and slow charge transfer rates of transition metal compounds drastically reduce capacitance at high current densities, limiting their practical applications in renewable energy systems [13–15].

Transition metal phosphides (TMPs) attract significant attention as alternatives to oxides and hydroxides due to their high electrical conductivity and good electrochemical properties [16,17]. TMPs are structurally similar to hydrogenase enzymes, where phosphorus acts as a hydride acceptor and transition metals as proton acceptors [16], making them promising catalysts for hydrodesulfurization [18] and hydrodenitrogenation [19], as well as suitable electrode materials for energy storage, for example Co_2P [20] and FeSnSbP [21]. It was recently found that one-dimensional (1D) NiCoP alloys possess high electrical conductivity and electrocatalytic properties suitable for Hydrogen Evolution Reaction (HER) application [22,23]. Electrochemical performance of TMPs in HER can be further enhanced by increasing surface roughness of catalytic nanoparticles [24] and oxygen doping to increase concentration of active sites [23]. Since their application in energy storage is rarely reported, it would be of interest to develop NiCoP compounds with electrochemical performance enhanced by a fine-tuned nano structure, as electrode materials for pseudocapacitors.

Plenty of void space is available in hollow-structured nanomaterials, with resulting high surface areas enhancing electrocatalytic activity in combination with hollow cores acting as volume buffers and storing electrolytes [25–27]. Recently, attention was paid to the development of nano-sized hollow-structured materials for electrochemical energy conversion and storage [28]. Many synthetic approaches have been proposed, among them hard templating method, utilizing a template compound which is subsequently selectively removed [29]. Due to complicated procedures and strongly corrosive chemicals which are usually required to remove the templates, there is a need for template-free and simple techniques to obtain hollow-structured nanomaterials, such as the ones utilizing Kirkendall effect which results from differences in atom diffusion rates at intermetallic interfaces [30–32]. Nano-sized hollow-structured CoP particles were successfully prepared in the mixture of actadecene, Co particles, trioctylphosphine and oleylamine [33]. NiCoP alloy exhibited high electrical conductivity and good electrochemical properties, making it attractive candidate for preparation of hollow-structure nanoparticles suitable for electrochemical energy storage applications.

In this study, a simple method was developed, for the first time, to synthesize 1D hollow-structured NiCoP nanorods via Kirkendall effect. The obtained NiCoP material exhibited high capacitance with good rate performance. An ASC cell using NiCoP as a cathode and AC as an anode demonstrated an energy density of 68 Wh kg^{-1} at a power density of 9594 W kg^{-1} and an energy density of 85 Wh kg^{-1} at a power density of 644.3 W kg^{-1}.

2. Experimental

2.1. Preparation of $NiCo_2O_4$ precursor

$Co(NO_3)_2$ (8 mmol), $Ni(NO_3)_2$ (4 mmol) and urea (12 mmol) were added into solution containing 30 ml of ethanol and 30 ml of water, followed by stirring at room temperature for 30 min. The solution was poured into a Teflon-lined autoclave, a piece of Ni foam (2×3 cm^2) was carefully placed inside, and the autoclave was heated at 150 °C for 6 h. Subsequently, Ni foam was rinsed with water and ethanol alternatively, and annealed at 350 °C for 2 h to oxidize Ni-Co layers formed on its surface.

2.2. Preparation of NiCoP

$NiCo_2O_4$ obtained in the previous step was phosphorized by placing NaH_2PO_2 upstream in the tube furnace that was heated up to 350 °C at a ramp of 5 °C min^{-1} and kept at this temperature for variable time periods under static N_2 atmosphere. The resulting materials, differing only by phosphorization times at 350 °C, were designated NiCoP.

2.3. Physical characterization

Crystal structure of as-prepared samples was studied on a Shimadzu XD-3A diffractometer where XRD patterns were recorded at 10° min^{-1} using Cu- Kα radiation with $\lambda = 0.15418$ nm. Their microstructure was investigated on a Carl Zeiss scanning electron microscope and a JEOL (JEM-2000 FX) transmission electron microscope. High angle annular dark field scanning transmission electron microscopy (STEM) images of the catalysts were taken using the same JEOL instrument operating at 200 kV. X-ray photoelectron spectroscopy (XPS) was carried out on a PHI-5702 spectrometer and C1 s peak at 285.0 eV was used as a reference for binding energies calibration.

2.4. Electrochemical measurements

Electrochemical performance of as-prepared NiCoP was studied using a CHI 660E electrochemical workstation. The experiments were carried out in a three-electrode configuration with a 1×1 cm^2 sample, which were measured by ruler, activated carbon (AC) and Hg/HgO (1.0 M KOH) serving as a working electrode, a counter electrode and a reference electrode respectively. Cyclic voltammetry (CV) graphs were recorded in a three- and a two-electrode systems in 1 M KOH aqueous electrolytes. Galvanostatic charge/discharge (GCD) and cycling tests were conducted using a LAND CT2001A battery measurement system. Areal specific capacity (C_a), energy density (E) and power density (P) were calculated according to the following equations:

$$C_a = 2I \times \int V\,dt/(A \times V) \tag{1}$$

$$E = C_m \times (\Delta V)^2/2 \tag{2}$$

$$P = E/\Delta t \tag{3}$$

where I, t, m, ΔV, and A represent discharge current (mA), discharge time (s), total mass of active materials (g), electrode potential window (V), and electrode surface area (cm^2) respectively.

Prior to assembly of the asymmetric supercapacitor, mass loadings of both cathode and anode were balanced according to the following equation [1,16]:

$$m^+/m^- = C^- \times \Delta E^-/(C^+ \times \Delta E^+) \tag{4}$$

where mass ratio of cathode to anode particles was set at 0.3.

3. Results and discussion

The microstructure of as-prepared NiCoP was firstly observed by scanning electron microscopy (SEM), as shown in Fig. 1a and b. Very even hair-like NiCoP nanorods have grown on the surface of Ni foam with no particles of different shapes visible. SEM images of NiCo precursor and $NiCo_2O_4$ shown in Fig. S1 reveal morphology almost identical to NiCoP samples (Fig. 1), indicating that heat treatment and subsequent phosphorization cause no damage to as-formed nanorods. Their detailed structure was further investigated by transmission electron microscopy (TEM). As shown in Fig. 1c–d, nanorods with bubble-like hollow structures, uniform diameters of ca. 75 nm and quite smooth surfaces were obtained. Well-defined lattice fringes are clearly visible in a high-resolution TEM image shown in

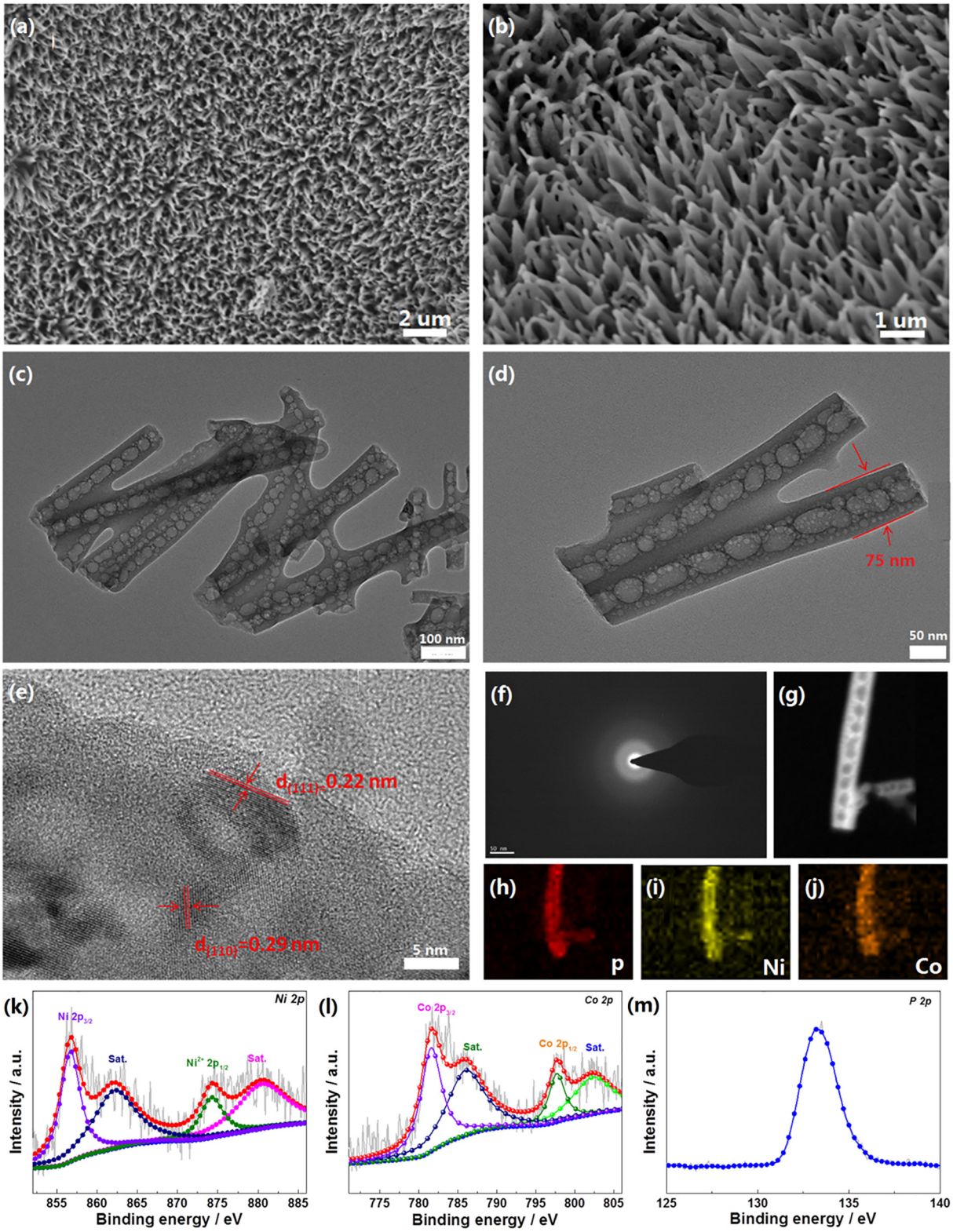

Fig. 1. (a, b) SEM images of NiCoP; (c–e) TEM images of NiCoP; (f) SAED pattern; (g–j) STEM mapping; deconvoluted high-resolution XPS spectra of Ni 2*p* (k), Co 2*p* (l), P 2p(m).

Fig. 1e where marked interplanar distances of 0.22 and 0.29 nm contribute to (110) and (111) planes of NiCoP, respectively [23]. According to electron energy loss spectroscopic mapping presented in Fig. 1g, elemental distribution of P, Ni and Co in the nanorods was quite even.

Figs. 1k–m and S2 present XPS investigation of NiCoP chemical state where the survey spectrum clearly shows signals of C 1s, Ni 2p, Co 2p and P 2p. Ni *2p* spectra could be fitted into two doublet peaks at ca. 874.3 eV and 856.7 eV with two satellites, which can be ascribed to Ni^{2+}, Ni^{3+} Ni-PO_x and Ni-P, indicating the formation of nickel phosphide. Co *2p* spectra of NiCoP samples were deconvoluted into two spin-orbit doublets as well as two satellites, formed due to the presence of Co^{2+} [34]. P *2p* spectra exhibit a peak at ca. 133.3 eV, which can be assigned to P in the phosphide. XPS results further confirm the

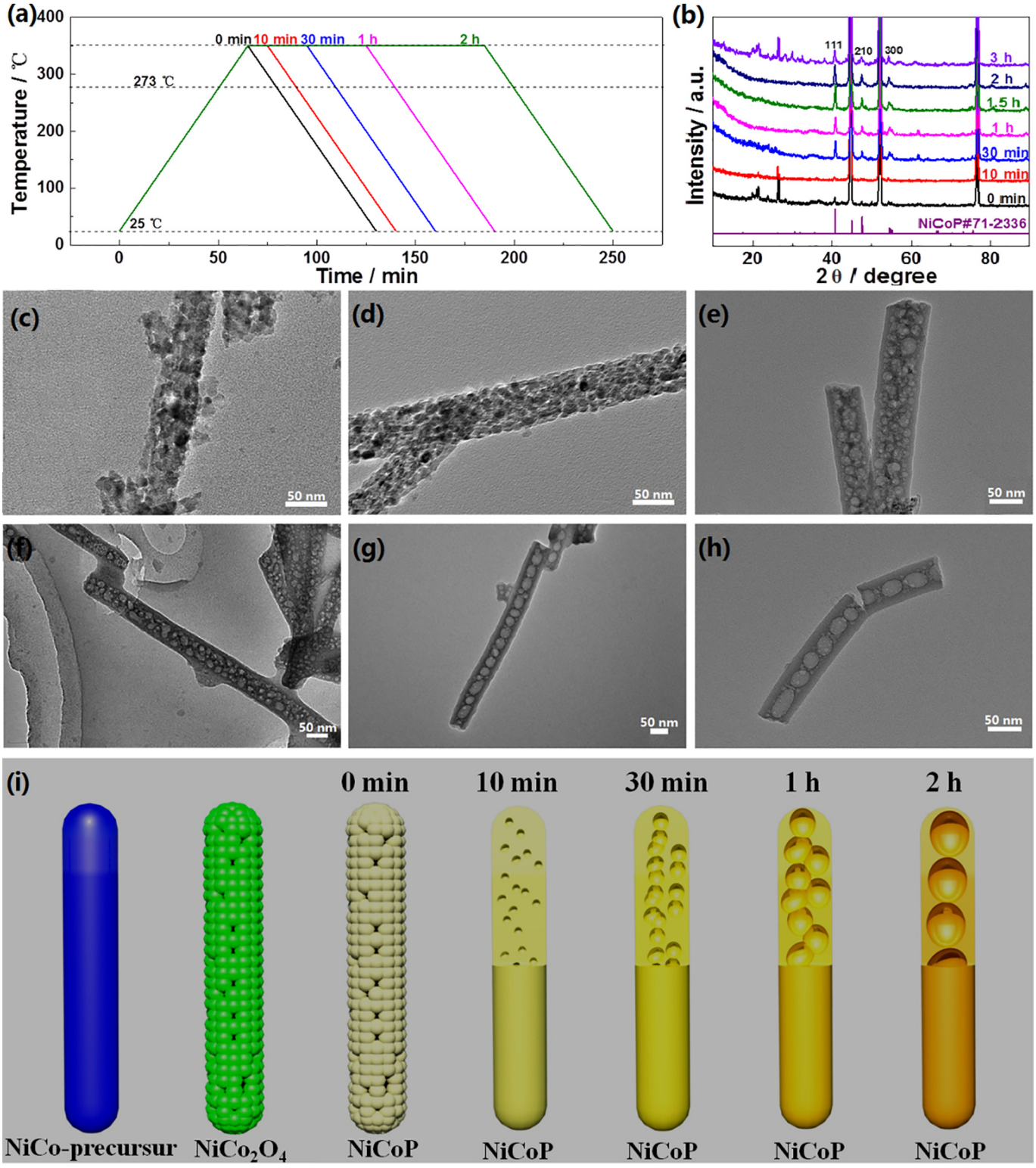

Fig. 2. (a) Schematic diagram of temperature rise rates; (b) NiCoP XRD patterns for different phosphorization times; (c) TEM images of pure $NiCo_2O_4$ after different phosphorization times of 0 min (d), 10 min (e), 30 min (f), 1 h (g), 2 h (h); (i) schematic diagram of phosphorization process.

formation of binary nickel and cobalt phosphides during the synthesis process.

Crystalline structure of as-prepared samples with various phosphorization times, graphically presented in Fig. 2a, was investigated by X-ray diffraction (XRD). As shown in Fig. 2b, phosphorization time significantly impacts crystallinity of the final products. For low phoshorization times, characteristic peaks of Ni foam at ca. 44.5, 52.0 and 76.5° are accompanied by very weak diffraction peaks of thin NiCoP layers on its surface. At phosphorization times longer than 30 min more NiCoP was formed, according to more pronounced peaks at ca. 40.98°, 47.56°, and 54.42°, corresponding to (111), (210) and (300) planes of hexagonal NiCoP. High purity of NiCoP phase formed on Ni foam is confirmed by the absence of diffraction peaks other than those attributed to NiCoP and Ni metal. However, when phosphorization time was further increased to 3 h, unidentified diffraction peaks at 20-35° appeared in the XRD pattern of NiCoP, revealing the crystalline structure change from hexagonal to a mixed one. This resulted in adoption of 2 h as optimal phosphorization time in this study. XRD spectra of NiCo precursor and $NiCo_2O_4$ shown in Figs. S3 and S4 can be interpreted in combination with TEM images of $NiCo_2O_4$ showing that nanorods with very rough surfaces were made of small particles, with no hollow structure present in them (Figs. 2c,

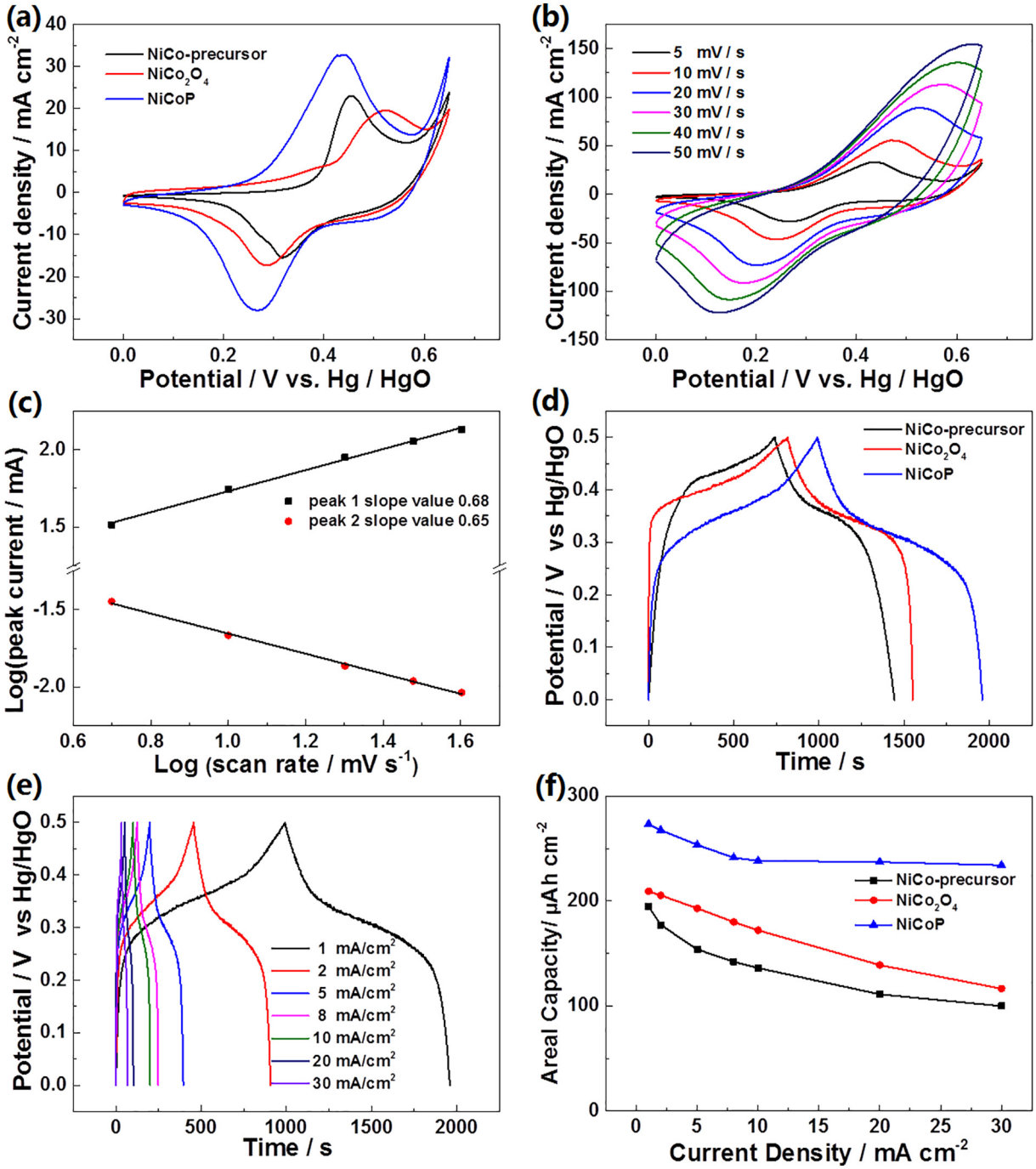

Fig. 3. (a) CV curves of NiCo-precursor, $NiCo_2O_4$ and NiCoP electrodes; (b) CV curves of NiCoP at various scan rates; (c) Power law dependence of current on sweep rate; (d) galvanostatic charge-discharge (GCD) curves of NiCo-precursor, $NiCo_2O_4$ and NiCoP electrodes; (e) GCD curves of NiCoP at different current densities; (f) area specific capacitance vs. current density for NiCo-precursor, $NiCo_2O_4$ and NiCoP.

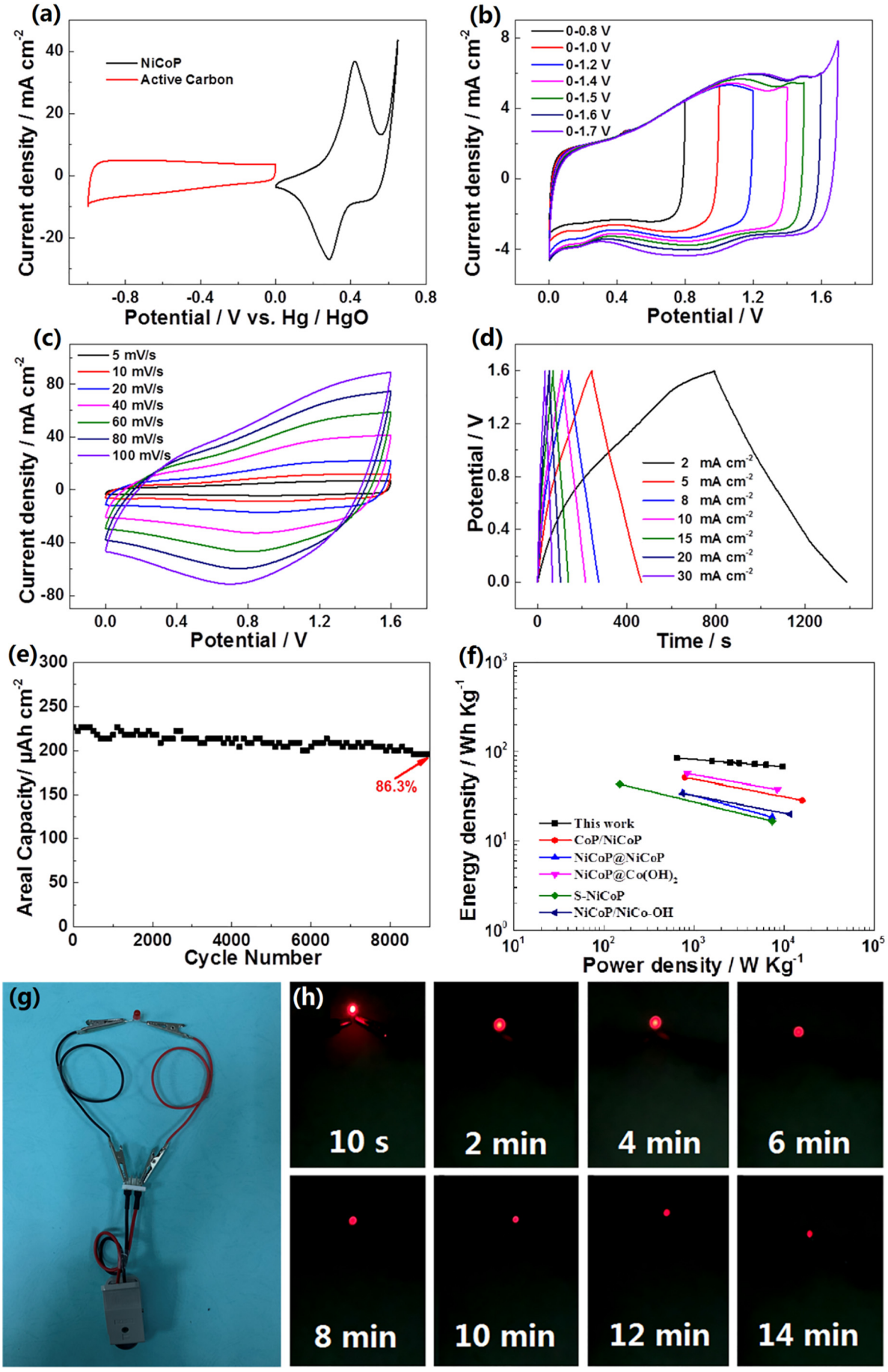
(a)
NiCoP
Active Carbon
Current density / mA cm-2
Potential / V vs. Hg / HgO
(b)
0-0.8 V
0-1.0 V
0-1.2 V
0-1.4 V
0-1.5 V
0-1.6 V
0-1.7 V
Current density / mA cm-2
Potential / V
(c)
5 mV/s
10 mV/s
20 mV/s
40 mV/s
60 mV/s
80 mV/s
100 mV/s
Current density / mA cm-2
Potential / V
(d)
2 mA cm-2
5 mA cm-2
8 mA cm-2
10 mA cm-2
15 mA cm-2
20 mA cm-2
30 mA cm-2
Potential / V
Time / s
(e)
86.3%
Areal Capacity/ μAh cm-2
Cycle Number
(f)
This work
CoP/NiCoP
NiCoP@NiCoP
NiCoP@Co(OH)2
S-NiCoP
NiCoP/NiCo-OH
Energy density / Wh Kg-1
Power density / W Kg-1
(g)
(h)
10 s
2 min
4 min
6 min
8 min
10 min
12 min
14 min

S5 and S6). After phosphorization at 350 °C, small particles visible in $NiCo_2O_4$ nanorods started to disappear and their rough surface became smoother with an increase in phosphorization time (Figs. 2d–h and S7–S10). At 10 min phosphorization time hollow structures started to appear in these nanorods and small "bubbles" could be observed with their sizes and quantity increasing gradually to the point where interconnected "bubbles" filled the nanorods complete after 1.5 h of phosphorization (Figs. 2g, h and S10). During this process, NaH_2PO_2 decomposed releasing phosphorus and hydrogen resulting in NiCoP formation on the surface of $NiCo_2O_4$. Due to its low diffusing rate, phosphorus penetrated through NiCoP layers very slowly, but hydrogen possessing much higher permeability easily went through to reduce $NiCo_2O_4$ to Ni and Co. At 350 °C these newly formed Ni and Co atoms are diffuse outwardly, penetrate NiCoP layers and react with phosphorus, resulting in the formation of hollow structures inside the nanorods [25,35]. Due to Kirkendall effect represented by different diffusion rates of Ni, Co and P, "bubbles" were formed as shown in Fig. 2i.

Electrochemical properties of as-prepared NiCoP were initially evaluated by cyclic voltammetry (CV) within a potential window of 0–0.7 V in KOH electrolyte. Two redox peaks clearly visible in CV curves of NiCo-precursor, $NiCo_2O_4$ and NiCoP (Fig. 3a) indicate pseudocapacitive nature of these materials in alkaline media. The integrated area of the NiCoP CV curve is much larger than those corresponding to NiCo-precursor and $NiCo_2O_4$ (Fig. 3a), indicating higher capacitance of NiCoP. Since Faradaic redox currents for NiCoP increased with an increase in scan rates (Fig. 3b), its charge store mechanism was further investigated using the equation $ip = av^b$ [36], where i_p represents peak current, a and b are adjustable parameters and v is scan rate. As shown in Fig. 3c, the straight line slope of peak 1 denotes the parameter b which can be used to determine the mechanism of processes occurring on NiCoP during charge and discharge, i.e. b of 0.5 represents a diffusion controlled- and b of 1.0 – a surface controlled process. A b value of 0.68 presented in Fig. 3c points to both diffusion- and surface-controlled electrochemical reactions taking place on NiCoP. CV curves at various scan rates retained almost initial shape without obvious distortion, indicating fast electron transfer kinetics.

Galvanostatic charge-discharge (GCD) experiments carried out on NiCo-precursor, $NiCo_2O_4$ and NiCoP reveal obvious potential plateaus occurring during both charge and discharge processes for all three materials, which demonstrates their battery-type properties [10]. Based on their GCD curves, capacitances of NiCo-precursor, $NiCo_2O_4$ and NiCoP samples were calculated to be 273.4, 209.3 and 190.4 μAh cm^{-2}, respectively, NiCoP capacitance being expectedly the highest. GCD curves of these three samples were also recorded at various current densities (Figs. 3e, S11a and S11b) and corresponding capacitances are shown in Fig. 3f. NiCoP capacitance of 273.4 μAh cm^{-2} at a current density of 1 mA cm^{-2} dropped to 234.2 μAh cm^{-2} when current density increased to 10 mA cm^{-2}. When current density went up to 30 mA cm^{-2}, capacitance declined slightly, indicating good electrical conductivity of NiCoP. Rising current density from 1 to 30 mA cm^{-2} resulted in capacitance retention of 85.6% for NiCoP, a much higher value than those of NiCo-precursor (51.4%) and $NiCo_2O_4$ (55.7%), indicating significant performance improvement achieved by phosphorization. Cycling stability of three materials was also studied by GCD at a current density of 20 mA cm^{-2} for 4000 cycles (Fig. S11f), and the NiCoP retained 82.1% of its initial capacitance after 4000 cycles.

To evaluate its electrochemical performance under real world conditions, NiCoP was used as a cathode and activated carbon (AC) as an anode to form asymmetric supercapacitor cell (ASC), in which KOH solution was used as an electrolyte. Suitable voltage window for this cell was evaluated by CV of NiCoP and AC at various potential ranges as shown in Fig. 4a, and voltage windows ranging from 0 to 0.8 to 0–1.7 V were initially selected. Obvious polarization visible in Fig. 4b at a voltage window of 0–1.7 V pointed to adoption of a narrower voltage window of 0–1.6 V. The CV curves possess rectangle-like shapes with very broad Faradaic redox currents, a typical manifestation of a pseudocapacitor utilizing Faradaic and electrical double-layer materials as electrodes [1]. CV of the ASC carried out at various scan rates revealed Faradaic reactions, such as Ni^{3+}/Ni^{2+}, occurring on NiCoP during both charge and discharge processes accompanied by adsorption/desorption and intercalation/deintercalation of OH^- ions on the electrode/electrolyte interface. In more detail, OH^- ions in the electrolyte move to the electrode to absorb/intercalate into it during negative potential scans and deintercalate/desorb and move back the electrolyte after polarity change. The ions, which have enough time to absorb on the electrode surface due to a slow scan rate, will be responsible for good reversible supercapacitor behaviour of the material, but the lack of time to absorb on the electrode at a high scan rate leads to distortion of rectangle-like CV shapes [37].

GCD of the ASC carried out over a current density range from 2 to 30 mA cm^{-2}, as shown in Fig. 4d, resulted in isosceles triangle curves, typical for a supercapacitor. An increase in current density resulted in the ASC specific capacitance dropping from 264.6 μAh cm^{-2} at 2 mA cm^{-2} to 213.2 μAh cm^{-2} at 30 mA cm^{-2}, which corresponds to 80.6% capacitance retention.

Cycling stability of the ASC was tested by continuous charge and discharge for 8000 cycles at a current density of 20 mA cm^{-2}. Fig. 4e shows that its specific capacity lost 13.7% after 8000 cycles, indicating its good cycling stability. Energy density vs. power density values were calculated and compared with representative samples reported in literature as shown in Fig. 4f. The ASC delivered a power density of 644.3 W kg^{-1} at an energy density of 85 Wh kg^{-1}, and 9594 Wh kg^{-1} at 68 W kg^{-1}. These numbers are quite high when compared with previously reported ASCs, such as CoP/NiCoP‖AC (51.6 Wh kg^{-1} at 800 W kg^{-1}) [38], NiCoP@ NiCoP‖AC (34.8 Wh kg^{-1} at 750.0 W kg^{-1}) [39], NiCoP@$NiCo(OH)_2$‖AC (57 Wh kg^{-1} at 850 W kg^{-1}) [40], S-NiCoP-2-300‖AC(43.54 Wh kg^{-1} at 150 W kg^{-1}) [41], NiCoP/NiCo-OH‖AC(34 Wh kg^{-1} at 755 W kg^{-1}) [42].

Two assembled ASCs were connected in series to illuminate red LED lights for longer than 14 min, further confirming their high energy density (Fig. 4g and h). Electrochemical results reported in this study demonstrate that 1D NiCoP nanorods with hollow structure can be considered promising nanomaterials for pseudocapacitor applications.

4. Conclusions

Hollow structured NiCoP nanorods were easily synthesized using Kirkendall effect owing to different diffusion rates of Ni, Co and P atoms. It was found that the hollow structure formed inside NiCoP nanorods could be efficiently tuned by controlling phosphorization time. Due to their good electrical conductivity, newly obtained hollow structured NiCoP nanorods exhibited a high capacity of 273.4 μAh cm^{-2} at a current density of 1 mA cm^{-2} with excellent rate performance. The nanorods also showed good functioning in a real ASC utilizing NiCoP as a cathode and AC as an anode. The ASC demonstrated a power density of 644.3 W kg^{-1} at an energy density of 85 Wh kg^{-1}, and an energy density of 9594 W kg^{-1} at a power density of 68 Wh kg^{-1}, demonstrating significant potential of hollow-structured NiCoP nanorods for practical application in electrochemical energy storage devices. In addition, the revealed mechanism of NiCoP hollow structure shows a way for fabricating porous structure of other phosphide.

Fig. 4. (a) CV curves of activated carbon anode and NiCoP; (b) CV curves of ASC measured at different operating voltages at 5 mV s^{-1}; (c) CV curves of ASC at different scan rates from 5 to 100 mV s^{-1}; (d) GCD curves of ASC at different current densities; (e) cycling stability of ASC at 20 mA cm^{-2}; (f) energy density vs. power density of NiCoP//AC cell, compared with other studies; (g,h) red LED powered by two series-connected coin cells after different illumination times.

CRediT authorship contribution statement

Zining Wang: Methodology, Validation, Writing - original draft. **Hui Wang:** Methodology, Validation, Writing - original draft. **Shan Ji:** Conceptualization, Resources, Writing - review & editing. **Xuyun Wang:** Visualization. **Pengxin Zhou:** Formal analysis. **Shuhui Huo:** Project administration. **Vladimir Linkov:** Writing - review & editing. **Rongfang Wang:** Conceptualization, Resources, Supervision.

Declaration of competing interest

The authors declare that this manuscript has not been submitted to other journals and there is no conflict of interest for this manuscript and that its submission is approved by all authors and tacitly or explicitly by the responsible authorities where the work was carried out. If accepted, it will not be published elsewhere in the same form, in English or in any other language, without the written consent of the publisher.

Acknowledgement

The authors would like to thank the National Natural Science Foundation of China (21766032 and 51661008) and Key Research and Development Program of Shandong Province of China (2019GGX103029) for financially supporting this work.

Appendix A. Supplementary data

Supplementary data to this article can be found online at https://doi.org/10.1016/j.matdes.2020.108807.

References

[1] C. Fangshuai, J. Shan, L. Quanbing, W. Hui, L. Hao, B.D.J. L., W. Guoxiu, W. Rongfang, Rational design of hierarchically core–shell structured Ni_3S_2@$NiMoO_4$ nanowires for electrochemical energy storage, Small 14 (2018), 1800791. .
[2] N.L. Wulan Septiani, Y.V. Kaneti, K.B. Fathoni, J. Wang, Y. Ide, B. Yuliarto, Nugraha, H.K. Dipojono, A.K. Nanjundan, D. Golberg, Y. Bando, Y. Yamauchi, Self-assembly of nickel phosphate-based nanotubes into two-dimensional crumpled sheet-like architectures for high-performance asymmetric supercapacitors, Nano Energy 67 (2020), 104270. .
[3] X. Zeng, L. Zhu, B. Yang, R. Yu, Necklace-like Fe_3O_4 nanoparticle beads on carbon nanotube threads for microwave absorption and supercapacitors, Mater. Des. 189 (2020) 108517.
[4] S. Sankar, A.T.A. Ahmed, A.I. Inamdar, H. Im, Y.B. Im, Y. Lee, D.Y. Kim, S. Lee, Biomass-derived ultrathin mesoporous graphitic carbon nanoflakes as stable electrode material for high-performance supercapacitors, Mater. Des. 169 (2019) 107688.
[5] W. Liu, M. Zhu, J. Liu, X. Li, J. Liu, Flexible asymmetric supercapacitor with high energy density based on optimized MnO_2 cathode and Fe_2O_3 anode, Chin. Chem. Lett. 30 (2019) 750–756.
[6] Z. Wang, H. Wang, S. Ji, H. Wang, D.J.L. Brett, R. Wang, Design and synthesis of tremella-like Ni-Co-S flakes on co-coated cotton textile as high-performance electrode for flexible supercapacitor, J. Alloys Compd. 814 (2020), 151789. .
[7] Y. Li, J. Henzie, T. Park, J. Wang, C. Young, H. Xie, J.W. Yi, J. Li, M. Kim, J. Kim, Y. Yamauchi, J. Na, Fabrication of flexible microsupercapacitors with binder-free ZIF-8 derived carbon films via electrophoretic deposition, Bull. Chem. Soc. Jpn. 93 (2020) 176–181.
[8] S. Makino, Y. Yamauchi, W. Sugimoto, Synthesis of electro-deposited ordered mesoporous RuO_x using lyotropic liquid crystal and application toward micro-supercapacitors, J. Power Sources 227 (2013) 153–160.
[9] R. Wang, Y. Ma, H. Wang, J. Key, D. Brett, S. Ji, S. Yin, P.K. Shen, A cost effective, highly porous, manganese oxide/carbon supercapacitor material with high rate capability, J. Mater. Chem. A 4 (2016) 5390–5394.
[10] F. Chen, H. Wang, S. Ji, B.G. Pollet, R. Wang, Hierarchical core-shell structured $CoNi_2S_4$/Ni_3S_2@$Ni(OH)_2$ nanosheet arrays as electrode for electrochemical energy storage, J. Alloys Compd. 785 (2019) 684–691.
[11] M. Cao, H. Wang, X. Wang, F. Chen, S. Ji, S. Pasupathi, R. Wang, Dual-shelled Cu_2O@Cu_9S_5@MnO_2 hollow spheres as advanced cathode material for energy storage, J. Alloys Compd. 805 (2019) 977–983.
[12] T. Nguyen, M. Boudard, M.J. Carmezim, M.F. Montemor, Layered $Ni(OH)_2$-$Co(OH)_2$ films prepared by electrodeposition as charge storage electrodes for hybrid supercapacitors, Sci. Rep. 7 (2017), 39980. .
[13] S.A. Pande, B. Pandit, B.R. Sankapal, Vanadium oxide anchored MWCNTs nanostructure for superior symmetric electrochemical supercapacitors, Mater. Des. 182 (2019) 107972.
[14] L.Y. Chen, J.L. Kang, Y. Hou, P. Liu, T. Fujita, A. Hirata, M.W. Chen, High-energy-density nonaqueous MnO2@nanoporous gold based supercapacitors, J. Mater. Chem. A 1 (2013) 9202–9207.
[15] Z. Wang, F. Chen, P. Kannan, S. Ji, H. Wang, Nickel phosphate nanowires directly grown on Ni foam as binder-free electrode for pseudocapacitors, Mater. Lett. 257 (2019), 126742. .
[16] M.A.A. Mohd Abdah, N.H.N. Azman, S. Kulandaivalu, Y. Sulaiman, Review of the use of transition-metal-oxide and conducting polymer-based fibres for high-performance supercapacitors, Mater. Des. 186 (2020) 108199.
[17] X.L. Chuanyin Xiong, Heguang Liu, Mengrui Li, Bingbing Li, Shasha Jiao, Wei Zhao, Chao Duan, Lei Dai, Yonghao Ni, Fabrication of 3D expanded graphite-based (MnO_2 nanowalls and PANI nanofibers) hybrid as bifunctional material for high-performance supercapacitor and sensor, J. Electrochem. Soc. 166 (2019) A3965–A3971.
[18] Z. Wang, H. Wang, S. Ji, X. Wang, B.G. Pollet, R. Wang, Multidimensional regulation of Ni_3S_2@$Co(OH)_2$ catalyst with high performance for wind energy electrolytic water, J. Power Sources 446 (2020), 227348. .
[19] T. Li, H. Jin, Z. Liang, L. Huang, Y. Lu, H. Yu, Z. Hu, J. Wu, B.Y. Xia, G. Feng, J. Zhou, Synthesis of single crystalline two-dimensional transition-metal phosphides via a salt-templating method, Nanoscale 10 (2018) 6844–6849.
[20] X. Chen, M. Cheng, D. Chen, R. Wang, Shape-controlled synthesis of Co_2P nanostructures and their application in supercapacitors, ACS Appl. Mater. Interfaces 8 (2016) 3892–3900.
[21] X.M. Zheng, L. Huang, Y. Xiao, H. Su, G.L. Xu, F. Fu, J.T. Li, S.G. Sun, A dicranopteris-like Fe-Sn-Sb-P alloy as a promising anode for lithium ion batteries, Chem. Commun. (Camb.) 48 (2012) 6854.
[22] P. Chen, T. Zhou, L. Xing, K. Xu, Y. Tong, H. Xie, L. Zhang, W. Yan, W. Chu, C. Wu, Y. Xie, Atomically dispersed iron–nitrogen species as electrocatalysts for bifunctional oxygen evolution and reduction reactions, Angew. Chem. Int. Ed. 56 (2017) 610–614.
[23] C. Liu, G. Zhang, L. Yu, J. Qu, H. Liu, Oxygen doping to optimize atomic hydrogen binding energy on NiCoP for highly efficient hydrogen evolution, Small 14 (2018) 1800421.
[24] X. Wang, R. Tong, Y. Wang, H. Tao, Z. Zhang, H. Wang, Surface roughening of nickel cobalt phosphide nanowire arrays/Ni foam for enhanced hydrogen evolution activity, ACS Appl. Mater. Interfaces 8 (2016) 34270–34279.
[25] R.M.R. Yadong Yin, Can K. Erdonmez, Steven Hughes, Gabor A. Somorjai, A. PaulAlivisatos, Formation of hollow nanocrystals through the nanoscale Kirkendall effect, Science 304 (2004) 711–714.
[26] T. Liu, L. Zhang, W. You, J. Yu, Core-Shell Nitrogen-Doped Carbon Hollow Spheres/Co3O4 Nanosheets as Advanced Electrode for HighPerformance Supercapacitor, Small 14 (2018) 1702407.
[27] W. Wang, M. Dahl, Y. Yin, Hollow nanocrystals through the nanoscale Kirkendall Effect, Chem. Mater. 25 (2012) 1179–1189.
[28] L. Yu, H. Hu, H.B. Wu, X.W. Lou, Complex hollow nanostructures: synthesis and energy-related applications, Adv. Mater. 29 (2017) 1604563.
[29] X.-Y. Yu, L. Yu, X.W. Lou, Metal sulfide hollow nanostructures for electrochemical energy storage, Adv. Energy Mater. 6 (2016), 1501333. .
[30] D. Ji, L. Fan, L. Tao, Y. Sun, M. Li, G. Yang, T.Q. Tran, S. Ramakrishna, S. Guo, The Kirkendall effect for engineering oxygen vacancy of hollow Co_3O_4 nanoparticles toward high-performance portable zinc-air batteries, Angew. Chem. Int. Ed. 58 (2019) 13840–13844.
[31] X. Zhang, C.Y. Chuah, P. Dong, Y.H. Cha, T.H. Bae, M.K. Song, Hierarchically porous co-MOF-74 hollow nanorods for enhanced dynamic CO_2 separation, ACS Appl. Mater. Interfaces 10 (2018) 43316–43322.
[32] Y. Son, Y. Son, M. Choi, M. Ko, S. Chae, N. Park, J. Cho, Hollow silicon nanostructures via the Kirkendall effect, Nano Lett. 15 (2015) 6914.
[33] E.J. Popczun, C.G. Read, C.W. Roske, N.S. Lewis, R.E. Schaak, Highly active electrocatalysis of the hydrogen evolution reaction by cobalt phosphide nanoparticles, Angew. Chem. Int. Ed. 53 (2014) 5427–5430.
[34] H. Wei, R. Chen, X. Wei, L. Zou, Q. Ni, D. Bao, CoNi2S4 nanosheet arrays supported on nickel foams with ultrahigh capacitance for aqueous asymmetric supercapacitor applications, ACS Appl. Mater. Interfaces 6 (2014), 19318. .
[35] K.N. Tu, U. Gösele, Hollow nanostructures based on the Kirkendall effect: design and stability considerations, Appl. Phys. Lett. 86 (2005), 093111. .
[36] B. Kirubasankar, S. Vijayan, S. Angaiah, Sonochemical synthesis of a 2D-2D $MoSe_2$/graphene nanohybrid electrode material for asymmetric supercapacitors, Sustain. Energ. Fuels 3 (2019) 467–477.
[37] S. Ji, Y. Ma, H. Wang, J. Key, D.J.L. Brett, R. Wang, Cage-like MnO_2-Mn_2O_3 hollow spheres with high specific capacitance and high rate capability as supercapacitor material, Electrochim. Acta 219 (2016) 540–546.
[38] Y. Lin, K. Sun, S. Liu, X. Chen, Y. Cheng, W.C. Cheong, Z. Chen, L. Zheng, J. Zhang, X. Li, Y. Pan, C. Chen, Construction of CoP/NiCoP nanotadpoles heterojunction interface for wide pH hydrogen evolution electrocatalysis and supercapacitor, Adv. Energy Mater. 9 (2019), 1901213. .
[39] Y. Zhu, Q. Zong, Q. Zhang, H. Yang, Q. Wang, H. Wang, Three-dimensional core-shell NiCoP@NiCoP array on carbon cloth for high performance flexible asymmetric supercapacitor, Electrochim. Acta 299 (2019) 441–450.
[40] X. Gao, Y. Zhao, K. Dai, J. Wang, B. Zhang, X. Shen, NiCoP nanowire@NiCo-layered double hydroxides nanosheet heterostructure for flexible asymmetric supercapacitors, Chem. Eng. J. 384 (2019), 123373. .
[41] X. Zhang, A. Wu, X. Wang, C. Tian, R. An, H. Fu, Porous NiCoP nanosheets as efficient and stable positive electrodes for advanced asymmetric supercapacitors, J. Mater. Chem. A 6 (2018) 17905–17914.
[42] X. Li, H. Wu, A.M. Elshahawy, L. Wang, S.J. Pennycook, C. Guan, J. Wang, Cactus-like NiCoP/NiCo-OH 3D architecture with tunable composition for high-performance electrochemical capacitors, Adv. Funct. Mater. 28 (2018) 1800036.